INTERNATIONAL JOURNAL FOR NUMERICAL METHODS IN FLUIDS
Int. J. Numer. Meth. Fluids 2006; **51**:939–961
Published online 24 November 2005 in Wiley InterScience (www.interscience.wiley.com). DOI: 10.1002/fld.1096

Numerical convergence of the MPFA O-method and U-method for general quadrilateral grids

I. Aavatsmark*,† and G. T. Eigestad‡

Center for Integrated Petroleum Research, University of Bergen, P.O. Box 7800, NO-5020 Bergen, Norway

SUMMARY

Control-volume discretization methods are applicable for problems that require good numerical approximations of fluxes. Here, a class of flux-continuous discretization methods, denoted multipoint flux approximation methods (MPFA), is discussed, and two different approaches are derived. The resulting discrete equations use pressures as the only unknowns, and the fluxes will be given explicitly as weighted sums of the discrete pressures. The two methods are denoted the O-method and the U-method, respectively, and differ in the way that continuity requirements are embedded in the discrete equations. Numerical tests are provided for smooth problems and problems with discontinuous coefficients for both the O-method and the U-method. Convergence rates of the methods are indicated through numerical experiments on smooth and rough grids. Copyright © 2005 John Wiley & Sons, Ltd.

KEY WORDS: control-volume discretization; anisotropy; inhomogeneity; convergence

1. INTRODUCTION

We consider a control-volume discretization of the model equations

$$\operatorname{div} \mathbf{q} = Q, \quad \mathbf{q} = -\mathbf{K} \operatorname{grad} u \tag{1}$$

on quadrilateral grids. The permeability $\mathbf{K}$ is required to be symmetric and positive definite. Our applications are flow in porous media, i.e. subsurface flow simulation. These equations contain an elliptic operator similar to the left-hand side of (1), and this motivates our study. The equations have properties which constrain the choice of grid and discretization technique used for the elliptic operator. For multiphase flow, some variables (saturations) behave like

*Correspondence to: I. Aavatsmark, Center for Integrated Petroleum Research, University of Bergen, P.O. Box 7800, NO-5020 Bergen, Norway.
†E-mail: ivar.aavatsmark@cipr.uib.no
‡E-mail: geir.eigestad@cipr.uib.no

Received 2 June 2005
Revised 30 August 2005
Accepted 30 August 2005

solutions of hyperbolic equations, while the pressure behaves like a solution of an elliptic equation. Phase transitions which are strongly pressure dependent, may occur.

Due to the hyperbolicity and the strongly nonlinear behaviour of the saturations, the discretization scheme should be locally conservative. Also, since the phase transitions are pressure dependent, the pressure should be evaluated at the same point as the saturations. This motivates the use of a control-volume scheme for (1), with evaluation of the dependent variable u at the centre of the cells.

Stability for the variables with hyperbolic behaviour may be accomplished by upstream weighting of the phase flow. In a fully implicit scheme for the flow equations, a simple upstream weighting can be achieved if the method for the elliptic operator in (1) yields the flux at the edges as an explicit function of the potential u at some neighbouring cell centres.

The absolute permeability may vary strongly in subsurface rocks. Since the potential node should be located at the cell centres, it is important that the discrete resistance between two nodes honours the strong heterogeneity.

The multipoint flux approximation (MPFA) methods are control-volume methods which are designed to satisfy the properties described above. The methods can be applied to quadrilateral grids [1–6] and to unstructured grids [2, 7–11], see References [1, 2] for a more complete bibliography.

Two different multipoint flux-approximation methods have been designed and are studied here: the O-method and the U-method. Also, different versions may be formulated [6, 12]. When formulated in physical space, the O-method is symmetric for parallelogram grids [4, 13]. For general grids it fails to be symmetric. The U-method, on the other hand, is only symmetric for uniform parallelogram grids on homogeneous media. The symmetric O-method has been proved to be convergent [14, 15]. In this paper we discuss the numerical convergence properties of the O- and the U-method for cases in which symmetry is not satisfied.

In Sections 2 and 3, the O-method and the U-method are derived, respectively, in an alternative, new way. The derivations are presented in two dimensions, and extensions to three dimensions are discussed. Convergence properties for both methods in two dimensions are discussed in Section 4, and results in three dimensions are presented for the O-method in Section 5. For related discussions of the numerical convergence, see also References [5, 6, 16–20].

2. THE O-METHOD

In this section the equations for the MPFA O-method in two dimensions are derived. Consider the four quadrilateral cells with a common vertex in Figure 1. The cells have cell centres $\mathbf{x}_k$, and the edges have midpoints $\bar{\mathbf{x}}_i$. The points are enumerated locally as shown in the figure. Lines are drawn between the cell centres and the midpoints of the edges (shown as dashed lines in the figure). These lines bound an area around each vertex which is called an *interaction volume* (also referred to as an interaction region in previous papers). Hence, the interaction volume in the figure is the polygon with corners $\mathbf{x}_1\bar{\mathbf{x}}_1\mathbf{x}_2\bar{\mathbf{x}}_4\mathbf{x}_4\bar{\mathbf{x}}_2\mathbf{x}_3\bar{\mathbf{x}}_3$ (Figure 2).

Within the interaction volume there are four half cell edges. Below, it will be shown how to determine the flux through these half edges from the interaction between the four cells. When the fluxes through the four half edges in an interaction volume around a vertex are determined, the procedure may be repeated for the interaction volumes of the other vertices.

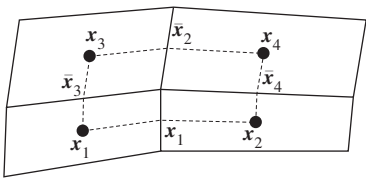

Figure 1. Interaction volume (bounded by the dashed lines).

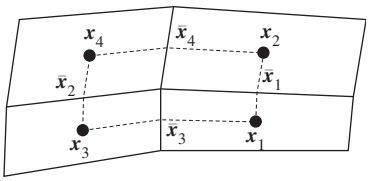

Figure 2. Cyclic renumbering of the points in Figure 1.

In this way, the flux through all the half edges in a grid will be determined. When the fluxes through the two half edges of an entire edge are known, they may be added to form an expression for the flux through the entire edge. An assembly procedure may then be performed to construct a system of difference equations corresponding to Equation (1).

This procedure also holds for the half edges at the boundary of a domain if the boundary conditions are given as homogeneous Neumann conditions. Outside the active cells a strip of artificial cells is put with vanishing permeability. The same procedure as described above for the interaction volumes around the vertices at the boundary, then gives the flux through the half edges at the boundary. More general boundary conditions are discussed in Reference [16].

We now show how the fluxes through the four half edges in an interaction volume may be determined. In each of the four cells of the interaction volume the potential u is expressed as a linear function. The value of the potential in each cell centre determines one of the coefficients in each cell for these linear functions. The linear function determines the flux through the half edges of the cell and the potential at the half edges. We require that the fluxes through the half edges in an interaction volume are continuous, and that the potentials at the midpoints of the edges are continuous. This yields eight equations for the determination of the unknown coefficients of the linear functions in the cells.

Every linear function is described by three coefficients in two dimensions, but one of them is already determined by the potential value at the cell centre. Altogether there are therefore eight unknown coefficients for the linear functions. They are determined by the eight continuity equations. Note that the continuity principles used here, are exactly the same as the principles used to derive the classical two-point flux formula [1].

Every cell is shared among four different interaction volumes. The representations of linear functions for the potential in a cell, may vary from interaction volume to interaction volume. This does not cause any difficulties, since the linear functions are only used to determine an

expression for the flux. In the resulting difference equations, only the potential value of the cell centres appears.

For each interaction volume, the linear functions in each cell may be determined in the following way. On a triangle with corners $\mathbf{x}_i$, $i = 1, 2, 3$, any linear function may be described by

$$u(\mathbf{x}) = \sum_{i=1}^{3} u_i \phi_i(\mathbf{x}) \tag{2}$$

Here, u_i is the value of $u(\mathbf{x})$ at vertex i, and $\phi_i(\mathbf{x})$ is the linear basis function defined by $\phi_i(\mathbf{x}_j) = \delta_{i,j}$. The gradient is easily calculated to be

$$\text{grad}\, \phi_i = -\frac{1}{2F}\mathbf{v}_i \tag{3}$$

where F is the area of the triangle, and $\mathbf{v}_i$ is the outer normal vector of the edge located opposite of vertex i, see Figure 3. The length of $\mathbf{v}_i$ equals the length of the edge to which it is normal. For these normal vectors the following relation holds:

$$\sum_{i=1}^{3} \mathbf{v}_i = \mathbf{0} \tag{4}$$

Thus, the gradient expression of the potential in the triangle may be written in the form

$$\text{grad}\, u = -\frac{1}{2F}\sum_{i=1}^{3} u_i \mathbf{v}_i = -\frac{1}{2F}[(u_2 - u_1)\mathbf{v}_2 + (u_3 - u_1)\mathbf{v}_3] \tag{5}$$

Now consider the grid cell in Figure 4. The grid cell has index k, and its centre is $\mathbf{x}_k$. Using local indices, the midpoints on the edges are denoted $\bar{\mathbf{x}}_1$ and $\bar{\mathbf{x}}_2$, and the associated normals on the connection lines between the cell centre and the midpoints of the edges are denoted $\mathbf{v}_2^{(k)}$ and $\mathbf{v}_1^{(k)}$, see Figure 4. Later, it will be suitable to let the vectors $\mathbf{v}_i^{(k)}$ point in the direction of increasing global cell indices. In this cell we therefore reverse the direction of these vectors. Using formula (5) on the triangle $\mathbf{x}_k\bar{\mathbf{x}}_1\bar{\mathbf{x}}_2$, yields

$$\text{grad}\, u = \frac{1}{2F_k}[\mathbf{v}_1^{(k)}(\bar{u}_1 - u_k) + \mathbf{v}_2^{(k)}(\bar{u}_2 - u_k)] \tag{6}$$

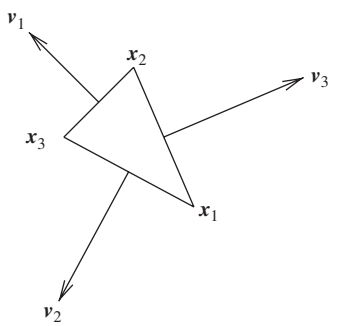

Figure 3. Triangle with edge normals $\mathbf{v}_i$.

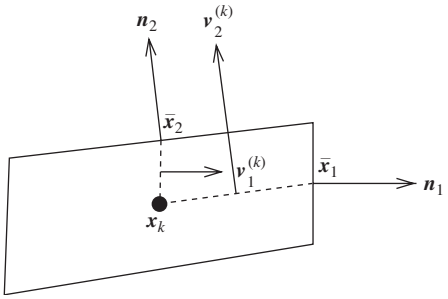

Figure 4. Normal vectors in cell k.

where $\bar{u}_i = u(\bar{\mathbf{x}}_i)$, $i = 1, 2$, and $u_k = u(\mathbf{x}_k)$. Each of the edges can be associated with a global direction, defined through the unit normal $\mathbf{n}_i$. It is convenient to also let $\mathbf{n}_i$ point in the direction of increasing global cell indices. The flux through half edge i as seen from cell k is denoted $f_i^{(k)}$, and may now be determined from the gradient of the potential in the cell. For the fluxes associated with the cell in Figure 4, the following expression appears:

$$\begin{bmatrix} f_1^{(k)} \\ f_2^{(k)} \end{bmatrix} = -\begin{bmatrix} \Gamma_1 \mathbf{n}_1^{\mathrm{T}} \\ \Gamma_2 \mathbf{n}_2^{\mathrm{T}} \end{bmatrix} \mathbf{K}_k \operatorname{grad} u$$

$$= -\frac{1}{2F_k} \begin{bmatrix} \Gamma_1 \mathbf{n}_1^{\mathrm{T}} \\ \Gamma_2 \mathbf{n}_2^{\mathrm{T}} \end{bmatrix} \mathbf{K}_k [\mathbf{v}_1^{(k)} \quad \mathbf{v}_2^{(k)}] \begin{bmatrix} \bar{u}_1 - u_k \\ \bar{u}_2 - u_k \end{bmatrix} \tag{7}$$

where Γ_i is the length of half edge i. By defining the matrix

$$\mathbf{G}_k = \frac{1}{2F_k} \begin{bmatrix} \Gamma_1 \mathbf{n}_1^{\mathrm{T}} \\ \Gamma_2 \mathbf{n}_2^{\mathrm{T}} \end{bmatrix} \mathbf{K}_k [\mathbf{v}_1^{(k)} \quad \mathbf{v}_2^{(k)}] = \frac{1}{2F_k} \begin{bmatrix} \Gamma_1 \mathbf{n}_1^{\mathrm{T}} \mathbf{K}_k \mathbf{v}_1^{(k)} & \Gamma_1 \mathbf{n}_1^{\mathrm{T}} \mathbf{K}_k \mathbf{v}_2^{(k)} \\ \Gamma_2 \mathbf{n}_2^{\mathrm{T}} \mathbf{K}_k \mathbf{v}_1^{(k)} & \Gamma_2 \mathbf{n}_2^{\mathrm{T}} \mathbf{K}_k \mathbf{v}_2^{(k)} \end{bmatrix} \tag{8}$$

Equation (7) may be written in the form

$$\begin{bmatrix} f_1^{(k)} \\ f_2^{(k)} \end{bmatrix} = -\mathbf{G}_k \begin{bmatrix} \bar{u}_1 - u_k \\ \bar{u}_2 - u_k \end{bmatrix} \tag{9}$$

Now consider the interaction volume in Figure 5. Here, the normal vectors of the edges are denoted $\mathbf{n}_1$, $\mathbf{n}_2$, $\mathbf{n}_3$, and $\mathbf{n}_4$. With these normal vectors, the matrix $\mathbf{G}_k$ is defined for all the four cells. Thus,

$$\begin{bmatrix} f_1^{(1)} \\ f_3^{(1)} \end{bmatrix} = -\mathbf{G}_1 \begin{bmatrix} \bar{u}_1 - u_1 \\ \bar{u}_3 - u_1 \end{bmatrix}, \quad \begin{bmatrix} f_1^{(2)} \\ f_4^{(2)} \end{bmatrix} = -\mathbf{G}_2 \begin{bmatrix} u_2 - \bar{u}_1 \\ \bar{u}_4 - u_2 \end{bmatrix} \tag{10}$$

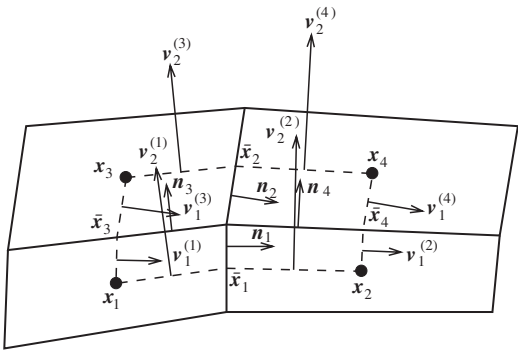

Figure 5. Normal vectors with local numbering in an interaction volume.

$$\begin{bmatrix} f_2^{(3)} \\ f_3^{(3)} \end{bmatrix} = -\mathbf{G}_3 \begin{bmatrix} \bar{u}_2 - u_3 \\ u_3 - \bar{u}_3 \end{bmatrix}, \quad \begin{bmatrix} f_2^{(4)} \\ f_4^{(4)} \end{bmatrix} = -\mathbf{G}_4 \begin{bmatrix} u_4 - \bar{u}_2 \\ u_4 - \bar{u}_4 \end{bmatrix} \tag{11}$$

Here, as before, $u_k = u(\mathbf{x}_k)$ and $\bar{u}_i = u(\bar{\mathbf{x}}_i)$, see Figure 5. Compared to cell 1, the directions of $\mathbf{v}_1^{(2)}$, $\mathbf{v}_2^{(3)}$, $\mathbf{v}_1^{(4)}$, and $\mathbf{v}_2^{(4)}$ have been reversed (see Figure 5). The differences $\bar{u}_1 - u_2$, $\bar{u}_3 - u_3$, $\bar{u}_2 - u_4$, and $\bar{u}_4 - u_4$ therefore appear in the expressions (10) and (11) with opposite sign.

The continuity conditions for the fluxes now yield

$$\begin{aligned} f_1 &= f_1^{(1)} = f_1^{(2)} \\ f_2 &= f_2^{(4)} = f_2^{(3)} \\ f_3 &= f_3^{(3)} = f_3^{(1)} \\ f_4 &= f_4^{(2)} = f_4^{(4)} \end{aligned} \tag{12}$$

Using expressions (10) and (11), these equations become

$$\begin{aligned} f_1 &= -g_{1,1}^{(1)}(\bar{u}_1 - u_1) - g_{1,2}^{(1)}(\bar{u}_3 - u_1) = g_{1,1}^{(2)}(\bar{u}_1 - u_2) - g_{1,2}^{(2)}(\bar{u}_4 - u_2) \\ f_2 &= g_{1,1}^{(4)}(\bar{u}_2 - u_4) + g_{1,2}^{(4)}(\bar{u}_4 - u_4) = -g_{1,1}^{(3)}(\bar{u}_2 - u_3) + g_{1,2}^{(3)}(\bar{u}_3 - u_3) \\ f_3 &= -g_{2,1}^{(3)}(\bar{u}_2 - u_3) + g_{2,2}^{(3)}(\bar{u}_3 - u_3) = -g_{2,1}^{(1)}(\bar{u}_1 - u_1) - g_{2,2}^{(1)}(\bar{u}_3 - u_1) \\ f_4 &= g_{2,1}^{(2)}(\bar{u}_1 - u_2) - g_{2,2}^{(2)}(\bar{u}_4 - u_2) = g_{2,1}^{(4)}(\bar{u}_2 - u_4) + g_{2,2}^{(4)}(\bar{u}_4 - u_4) \end{aligned} \tag{13}$$

Equations (13) contain the edge values $\bar{u}_1$, $\bar{u}_2$, $\bar{u}_3$, and $\bar{u}_4$. Tacitly we have here used the same expression for the edge value of the cells at each side of an edge, and thereby implicitly demanded continuity for the potential at the points $\bar{\mathbf{x}}_1$, $\bar{\mathbf{x}}_2$, $\bar{\mathbf{x}}_3$ and $\bar{\mathbf{x}}_4$.

If the matrix $\mathbf{G}_k$ is diagonal for all cell indices k, the grid is called **K**-orthogonal. The system of equations (13) is then no longer coupled, and the flux through the edges can be

determined by eliminating the edge values $\bar{u}_i$. This gives a two-point flux expression. If the grid is not **K**-orthogonal, the edge values $\bar{u}_i$ may still be eliminated in each interaction volume. The procedure is described in the following way:

The fluxes of the system of equations (13) can be collected in the vector **f** defined by $\mathbf{f} = [f_1, f_2, f_3, f_4]^{\mathrm{T}}$. The system of equations further contains the potential values of the cell centres $\mathbf{u} = [u_1, u_2, u_3, u_4]^{\mathrm{T}}$ and the potential values at the midpoints of the cell edges $\mathbf{v} = [\bar{u}_1,\ \bar{u}_2,\ \bar{u}_3,\ \bar{u}_4]^{\mathrm{T}}$. The expressions on each side of the left equality sign of (13) can therefore be written in the form

$$\mathbf{f} = \mathbf{C}\mathbf{v} + \mathbf{F}\mathbf{u} \tag{14}$$

The expressions on each side of the right equality sign in the system of equations (13) may after a reorganization be written in the form

$$\mathbf{A}\mathbf{v} = \mathbf{B}\mathbf{u} \tag{15}$$

Hence, **v** may be eliminated by solving Equation (15) with respect to **v** and substituting $\mathbf{v} = \mathbf{A}^{-1}\mathbf{B}\mathbf{u}$ into (14). This gives the flux expression

$$\mathbf{f} = \mathbf{T}\mathbf{u} \tag{16}$$

where

$$\mathbf{T} = \mathbf{C}\mathbf{A}^{-1}\mathbf{B} + \mathbf{F} \tag{17}$$

The entries of the matrix **T** are called *transmissibility coefficients*. Equation (16) gives the flux through the half edges expressed by the potential values at the cell centres of an interaction volume.

Having determined the flux expression for all half edges, the two flux expressions of the two half edges which constitute an edge, can be added. This is shown in Figure 6, where the cells 1, 2, 3, and 4 constitute one interaction volume, and the cells 1, 2, 5, and 6 constitute the other. The flux stencil of the edge between cell 1 and 2 will therefore consist of the six cells of the figure. When the flux expressions have been found, these may be used in a discrete version of Equation (1). For the cell shown in Figure 7, this yields the equation

$$\bar{f}_1 + \bar{f}_2 - \bar{f}_3 - \bar{f}_4 = VQ \tag{18}$$

where $\bar{f}_i$ is the flux through the entire edge i, V is the volume of the cell, and Q has been approximated by a constant in the cell. This is a difference equation with u at the cell centres as the unknowns.

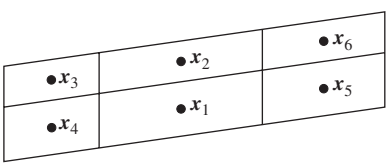

Figure 6. Flux stencil.

If two neighbouring cells have vanishing permeability, the corresponding row in the matrix **A** vanishes, and hence, the matrix **A** is singular. Because there is no need to determine the flux across the interfaces of cells with vanishing permeability, the system may be reduced, and this will remove the singularity. However, it is more favourable to retain the system of unknowns and redefine the matrix **A** such that it becomes nonsingular. This is easily done by setting the diagonal elements of the vanishing rows in the matrix **A** equal to 1. The new system of equations has the same transmissibility coefficients as the reduced system for the interfaces between cells with nonvanishing permeability.

If cell k in Figure 4 is a parallelogram, the expression for the matrix $\mathbf{G}_k$, Equation (8), is simplified. For a parallelogram-shaped cell with index k, we denote the normal vectors of the edges with $\mathbf{a}_i^{(k)}$, $i=1,2$. These have lengths equal to the length of the edges. The normal vectors are shown in Figure 8. Obviously, $\Gamma_i \mathbf{n}_i = \mathbf{a}_i^{(k)}/2$ and $\mathbf{v}_i^{(k)} = \mathbf{a}_i^{(k)}/2$. Further, $F_k = V_k/8$, where V_k is the area of cell k. It follows that for a parallelogram-shaped cell

$$\mathbf{G}_k = \frac{1}{V_k}[\mathbf{a}_1^{(k)} \quad \mathbf{a}_2^{(k)}]^{\mathrm{T}} \mathbf{K}_k [\mathbf{a}_1^{(k)} \quad \mathbf{a}_2^{(k)}] \tag{19}$$

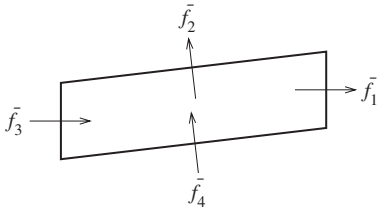

Figure 7. Flux through the cell edge of a cell.

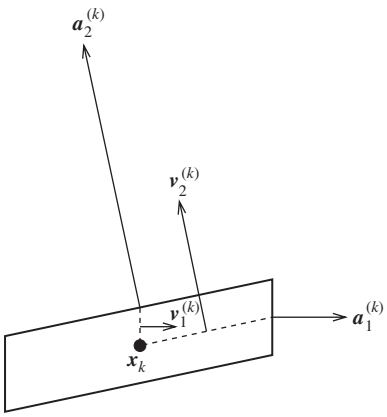

Figure 8. Normal vectors in parallelogram cells.

Letting $\mathbf{J}_k = [\mathbf{a}_1^{(k)},\ \mathbf{a}_2^{(k)}]$, it follows that $V_k = |\det \mathbf{J}_k|$, and Equation (19) becomes

$$\mathbf{G}_k = \frac{1}{|\det \mathbf{J}_k|}\,\mathbf{J}_k^{\mathrm{T}}\mathbf{K}_k\mathbf{J}_k \tag{20}$$

Hence, for a parallelogram cell the tensor $\mathbf{G}_k$ is symmetric. Equation (20) is a congruence transformation. Thus, the tensor $\mathbf{G}_k$, as given by (19), is symmetric and positive definite if and only if $\mathbf{K}_k$ has these properties. If the tensor $\mathbf{G}_k$ is diagonal for all cell indices k, i.e. if

$$(\mathbf{a}_i^{(k)})^{\mathrm{T}}\mathbf{K}_k\mathbf{a}_j^{(k)} = 0, \quad i \neq j \tag{21}$$

then the grid is **K**-orthogonal.

In the matrix $\mathbf{G}_k$ it is sometimes useful to perform a splitting, such that anisotropy and grid skewness appear in one matrix and the mesh distances in another. If $\Delta\eta_k$ is the length of $\mathbf{a}_1^{(k)}$ and $\Delta\xi_k$ is the length of $\mathbf{a}_2^{(k)}$, then for a parallelogram grid,

$$\mathbf{G}_k = \frac{1}{\Delta\xi_k\Delta\eta_k}\mathbf{D}_k\mathbf{H}_k\mathbf{D}_k \tag{22}$$

where

$$\begin{aligned}\mathbf{H}_k &= \frac{1}{\det[\mathbf{n}_1, \mathbf{n}_2]}[\mathbf{n}_1 \quad \mathbf{n}_2]^{\mathrm{T}}\mathbf{K}_k[\mathbf{n}_1 \quad \mathbf{n}_2] \\ &= \frac{1}{\det[\mathbf{n}_1, \mathbf{n}_2]}\begin{bmatrix}\mathbf{n}_1^{\mathrm{T}}\mathbf{K}_k\mathbf{n}_1 & \mathbf{n}_1^{\mathrm{T}}\mathbf{K}_k\mathbf{n}_2 \\ \mathbf{n}_2^{\mathrm{T}}\mathbf{K}_k\mathbf{n}_1 & \mathbf{n}_2^{\mathrm{T}}\mathbf{K}_k\mathbf{n}_2\end{bmatrix}\end{aligned} \tag{23}$$

and

$$\mathbf{D}_k = \mathrm{diag}(\Delta\eta_k,\ \Delta\xi_k) \tag{24}$$

Here, $\mathbf{n}_i$ is the unit normal vector which is parallel with $\mathbf{a}_i^{(k)}$, see Figure 8. If $\mathbf{H}_k$ is diagonal, the grid is **K**-orthogonal.

2.1. Extension to three dimensions

The principles of the MPFA O-method carry over to three dimensions in a straightforward manner. In three dimensions, an interaction volume contains 8 subcells and 12 interfaces, see Figure 9. The linear functions in the eight cells are described by 32 coefficients. Eight of these are determined by the potential values at the cell centres. The rest of them are determined by the two continuity conditions at each of the 12 interfaces: the flux is required to be continuous at the interfaces, and the potential is required to be continuous at the interface midpoints.

The generalization of the equations of Section 2 to three dimensions is straightforward. However, a three-dimensional cell described by its eight corners, generally does not have planar surfaces. The unit normal vector $\mathbf{n}_i$ of an interface is therefore not a constant across the interface. This can be accounted for by integrating the normal vector over the interface of the subcell in question.

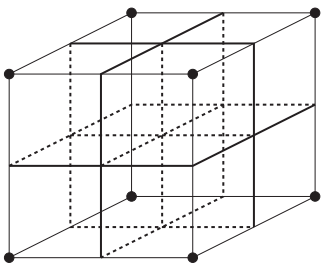

Figure 9. Three-dimensional interaction volume (bold lines) with 8 subcells and 12 interfaces (thick lines).

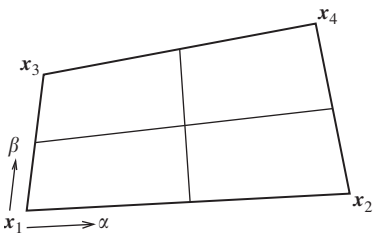

Figure 10. Bilinear coordinates of a surface.

To determine this integral, consider the interface in Figure 10. Let the corners of the interface be $\mathbf{x}_k$, $k=1,\ldots,4$, and let the surface which is spanned by these points, be described by the bilinear function

$$\mathbf{x}(\alpha,\beta)=\beta\big(\alpha\mathbf{x}_4+(1-\alpha)\mathbf{x}_3\big)+(1-\beta)(\alpha\mathbf{x}_2+(1-\alpha)\mathbf{x}_1) \tag{25}$$

where $(\alpha,\beta)\in[0,1]\times[0,1]$. The corners $\mathbf{x}_i$, $i=1,2,3,4$, may not lie in the same plane. We now calculate the surface integral $\hat{\mathbf{n}}=\int_S \mathbf{n}\,\mathrm{d}\sigma$, where S is the surface given by $\alpha\leqslant\frac{1}{2}$ and $\beta\leqslant\frac{1}{2}$. This surface is the lower left quarter in Figure 10. A straightforward integration gives

$$\begin{aligned}
\hat{\mathbf{n}}&=\int_S \mathbf{n}\,\mathrm{d}\sigma=\int_0^{1/2}\int_0^{1/2}\left(\frac{\partial\mathbf{x}}{\partial\alpha}\times\frac{\partial\mathbf{x}}{\partial\beta}\right)\mathrm{d}\alpha\,\mathrm{d}\beta\\
&=\int_0^{1/2}\int_0^{1/2}[\beta(\mathbf{x}_4-\mathbf{x}_3)+(1-\beta)(\mathbf{x}_2-\mathbf{x}_1)]\\
&\quad\times[\alpha(\mathbf{x}_4-\mathbf{x}_2)+(1-\alpha)(\mathbf{x}_3-\mathbf{x}_1)]\,\mathrm{d}\alpha\,\mathrm{d}\beta\\
&=\frac{1}{64}[9(\mathbf{x}_2-\mathbf{x}_1)\times(\mathbf{x}_3-\mathbf{x}_1)+3(\mathbf{x}_2-\mathbf{x}_1)\times(\mathbf{x}_4-\mathbf{x}_2)\\
&\quad+3(\mathbf{x}_4-\mathbf{x}_3)\times(\mathbf{x}_3-\mathbf{x}_1)+(\mathbf{x}_4-\mathbf{x}_3)\times(\mathbf{x}_4-\mathbf{x}_2)]
\end{aligned} \tag{26}$$

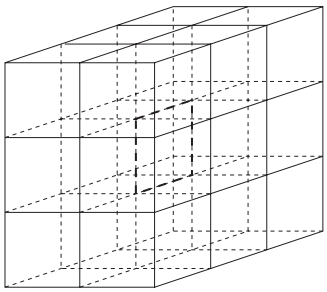

Figure 11. Flux stencil of an interface (bold) for the O-method in 3D.

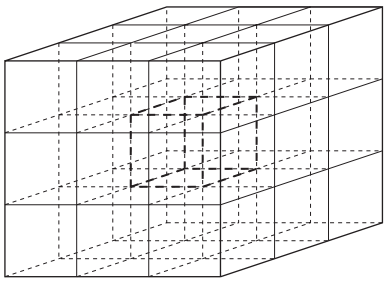

Figure 12. Cell stencil of a cell (bold) for the O-method in 3D.

The quantity $\hat{\mathbf{n}}$ is the integrated normal vector over the interface of the subcell at the corner $\mathbf{x}_1$. The vector $\hat{\mathbf{n}}$ has length equal to the area of the subcell interface.

In the three-dimensional O-method, the flux stencil contains 18 cells (see Figure 11), and the cell stencil contains 27 cells (see Figure 12).

3. THE U-METHOD

In this section we derive the MPFA *U-method*. This method is defined by the following conditions. As for the O-method, the potential is written as a linear function in every cell of the interaction volume. However, the conditions at the cell edges are different. To determine the flux through the half edge at $\bar{\mathbf{x}}_1$ in Figure 13, the following continuity conditions are used. It is required that the fluxes through the edges at the points $\bar{\mathbf{x}}_1$, $\bar{\mathbf{x}}_3$ and $\bar{\mathbf{x}}_4$ are continuous. Further, the potential at $\bar{\mathbf{x}}_1$ has to be continuous. These conditions are the same conditions as for the O-method. However, for the edges at the points $\bar{\mathbf{x}}_3$ and $\bar{\mathbf{x}}_4$, it is required that the potential along the entire half edge is continuous. For each of these edges, this requirement yields two continuity conditions for the potential.

As for the O-method, the linear functions of the U-method have $4 \cdot 3 = 12$ coefficients in the interaction volume. Four of these coefficients are determined by the potential values in

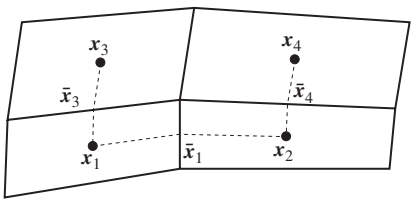

Figure 13. Interaction lines of the U-method (dashed).

the cell centres of the four cells. The remaining eight coefficients are determined by the three flux continuity conditions and the five potential continuity conditions.

The system of equations described above, only determines the flux through the half edge given by $\bar{\mathbf{x}}_1$ and the common vertex. To determine the fluxes through the other half edges in the interaction volume, the procedure must be repeated for every half edge in the interaction volume. This means that in the U-method, the linear functions of the subcells in the interaction volume change from one half-edge evaluation to the next half-edge evaluation.

The letters O and U in the names of the methods come from the dashed lines in Figures 1 and 13. In Figure 1 the dashed lines, which indicate the interactions between the cells, constitute a stylized O. In Figure 13 the same interaction lines constitute a stylized U.

To express the continuity conditions of the U-method, the same expressions as in Section 2 are applied. However, since no continuity at $\bar{\mathbf{x}}_2$ is required, the potential u may now have different values at $\bar{\mathbf{x}}_2$ on each side of the edge. This is denoted by the superscripts (3) and (4), respectively. Instead of the flux expressions (11), the following expressions are now applied

$$\begin{bmatrix} f_2^{(3)} \\ f_3^{(3)} \end{bmatrix} = -\mathbf{G}_3 \begin{bmatrix} \bar{u}_2^{(3)} - u_3 \\ u_3 - \bar{u}_3 \end{bmatrix}, \quad \begin{bmatrix} f_2^{(4)} \\ f_4^{(4)} \end{bmatrix} = -\mathbf{G}_4 \begin{bmatrix} u_4 - \bar{u}_2^{(4)} \\ u_4 - \bar{u}_4 \end{bmatrix} \tag{27}$$

The flux continuity conditions to determine the flux through the half edge at $\bar{\mathbf{x}}_1$ then read

$$\begin{aligned} f_1 &= f_1^{(1)} = f_1^{(2)} \\ f_3 &= f_3^{(3)} = f_3^{(1)} \\ f_4 &= f_4^{(2)} = f_4^{(4)} \end{aligned} \tag{28}$$

The quantities which are used in these equations, are given in (10) and (27). As in Section 2, the continuity of the potential at the points $\bar{\mathbf{x}}_1$, $\bar{\mathbf{x}}_3$ and $\bar{\mathbf{x}}_4$ are contained here. To insure the continuity of the potentials along the two half edges at $\bar{\mathbf{x}}_3$ and $\bar{\mathbf{x}}_4$, the potential function in all the cells are needed. For cell k in Figure 4, the gradient is given by Equation (6). Hence, the linear function is expressed by

$$\begin{aligned} u^{(k)}(\mathbf{x}) &= u_k + (\mathbf{x} - \mathbf{x}_k)\,\mathrm{grad}\,u^{(k)} \\ &= u_k + \frac{1}{2F_k}(\mathbf{x} - \mathbf{x}_k)^{\mathrm{T}}[\mathbf{v}_1^{(k)} \quad \mathbf{v}_2^{(k)}] \begin{bmatrix} \bar{u}_1 - u_k \\ \bar{u}_2 - u_k \end{bmatrix} \end{aligned} \tag{29}$$

The linear functions of all the cells in Figure 5 may be expressed in this way. The remaining potential continuity conditions read

$$\begin{aligned} u^{(1)}(\bar{\mathbf{x}}_5) &= u^{(3)}(\bar{\mathbf{x}}_5) \\ u^{(2)}(\bar{\mathbf{x}}_6) &= u^{(4)}(\bar{\mathbf{x}}_6) \end{aligned} \tag{30}$$

where $\bar{\mathbf{x}}_5 \neq \bar{\mathbf{x}}_3$ is any point on the edge between the cells 1 and 3, and $\bar{\mathbf{x}}_6 \neq \bar{\mathbf{x}}_4$ is any point on the edge between the cells 2 and 4.

The system of equations (28), (30) may be treated in the same way as the system of equations in Section 2. The unknown potential values at the edges are assembled in the vector $\mathbf{v} = [\bar{u}_1, \bar{u}_2^{(3)}, \bar{u}_2^{(4)}, \bar{u}_3, \bar{u}_4]^{\mathrm{T}}$, whereas the potential values of the cell centres as before are given by the vector $\mathbf{u} = [u_1, u_2, u_3, u_4]^{\mathrm{T}}$. The system of equations is written in the form $\mathbf{Av} = \mathbf{Bu}$, and the solution $\mathbf{v} = \mathbf{A}^{-1}\mathbf{Bu}$ is substituted into the flux expression $\mathbf{f} = \mathbf{Cv} + \mathbf{Fu}$, where $\mathbf{f} = [f_1, f_2, f_3]^{\mathrm{T}}$. However, in the resulting matrix $\mathbf{T} = \mathbf{CA}^{-1}\mathbf{B} + \mathbf{F}$, only the first row is used. The flux expressions corresponding to the last two rows of $\mathbf{T}$ are not used.

To determine the flux expressions of the other half-edges in Figure 1, the procedure must be repeated with interchanged continuity conditions. This may be accomplished by a renumbering of the points in Figure 1. For example, to determine the flux through the half edge associated with $\bar{\mathbf{x}}_4$ in Figure 1, all the points may be cyclically renumbered, as shown in Figure 2. With the new numbering the procedure described above yields the flux expression for the half edge associated with $\bar{\mathbf{x}}_1$ in Figure 2.

When all the flux expressions for the half edges in the grid have been found, the flux expressions for the entire edges are determined by assembling half-edge fluxes as for the O-method. The flux stencil of an entire edge contains six cells, and the cell stencil contains nine cells.

If the grid is $\mathbf{K}$-orthogonal, Equations (28) are decoupled. As for the O-method, the usual two-point flux approximation then appears.

3.1. Extension to three dimensions

The U-method can be extended to three dimensions. When the flux through the quarter interface which is shaded in Figure 14, is to be determined, the following continuity conditions for the shown interfaces are applied. The flux must be continuous at all of the five interfaces. At the corner of the shading (i.e. at the midpoint of the cell surface) the potential must be continuous. At the other four interfaces, the potential must be continuous along the entire surface. The linear functions of the six cells have $6 \cdot 4 = 24$ degrees of freedom. Six of them are

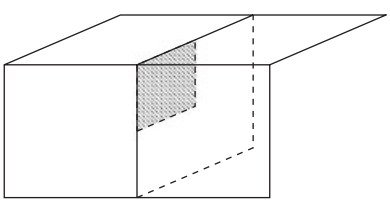

Figure 14. Edges with continuity conditions for the U-method in 3D.

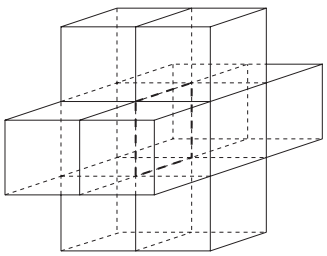

Figure 15. Flux stencil of an interface (bold) for the U-method in 3D.

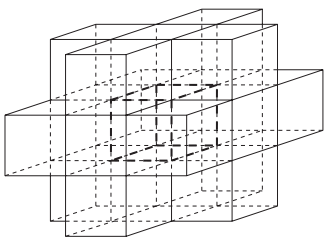

Figure 16. Cell stencil of a cell (bold) for the U-method in 3D.

determined by the potential values at the cell centres. The remaining 18 degrees of freedom are determined by the above continuity requirements.

In the three-dimensional U-method, the flux stencil contains 10 cells (see Figure 15), and the cell stencil contains 19 cells (see Figure 16).

4. TWO-DIMENSIONAL RESULTS

Convergence has been proved for a symmetric version of the MPFA O-method [14, 15]. However, the proved error bounds are not sharp. Also, the convergence properties of the nonsymmetric version of the O-method (i.e. the O-method in physical space as described in Section 2) are better [5].

In this section we compare numerical convergence properties of the MPFA O-method and U-method on quadrilateral grids. Both methods yield in general a nonsymmetric method. For all test cases, we compute the discrete L^2 norm of the error. This norm is defined in Reference [16]. For bounded solutions, we also compute the L^∞ norm of the error. The convergence rate for the O-method has previously been reported for smooth grids in Reference [16] and for rough grids in Reference [5]. See also References [6, 18].

Three groups of test cases are considered. All cases are simulated on the grid shown in Figure 17(a). The boundary conditions are given by Dirichlet conditions, and are implemented by interpolation. In field applications, the grids are rough, and to test the robustness of the methods on such grids, the grid points are perturbed by a random displacement of $\mathcal{O}(h)$. This

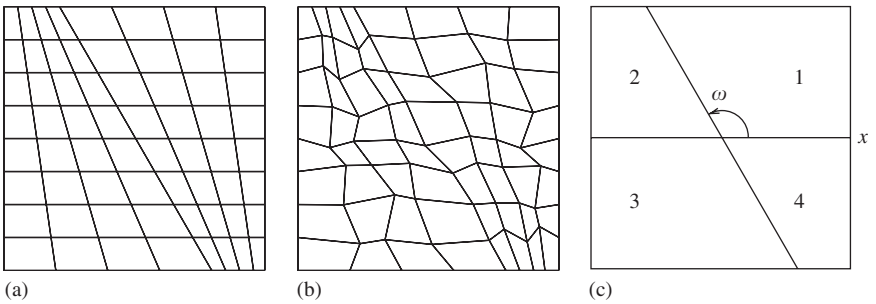

Figure 17. Simulation grids and domain: (a) smooth grid; (b) rough grid; and (c) corner with regions.

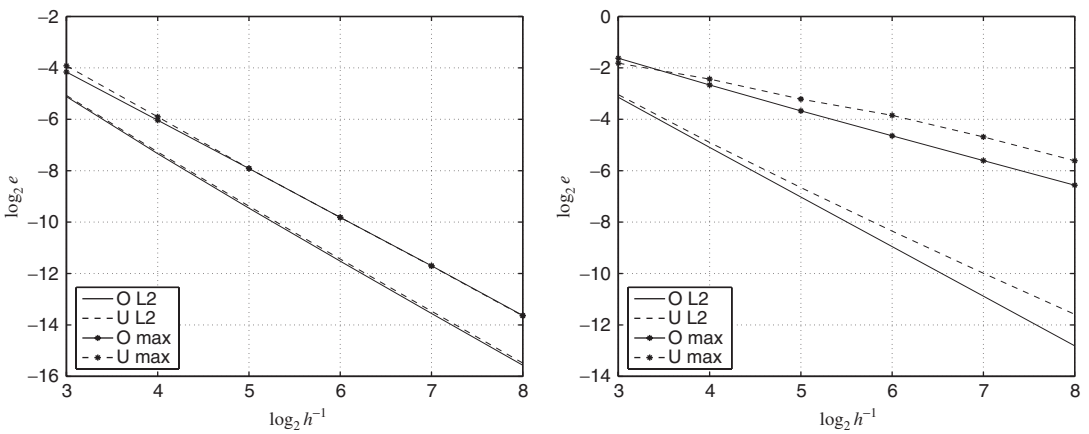

Figure 18. Convergence behaviour for the smooth solution (31) on smooth grids.
Left: Pressure. Right: Edge normal flow densities.

perturbation is performed on each refinement level. A rough grid is shown in Figure 17(b). A precise definition of smooth and rough grids is not given here, but earlier testing [5] has shown that $\mathcal{O}(h^2)$ perturbations of the grid shown in Figure 17(a) yield the same convergence properties as the unperturbed grid.

Note that, since the perturbations are random, all the rough grids are different. This also holds for the solutions shown in the same plot. Hence, for the rough grids, a comparison of solutions at the same refinement level must be done with some caution.

The first test cases are performed with the solution

$$u(x, y) = \cosh(\pi x)\cos(\pi y) \tag{31}$$

of the problem (1) on an isotropic, homogeneous medium.

The test results are shown in Figure 18 for the smooth grids and in Figure 19 for the rough grids. For the pressure, the convergence rate is the same for the O-method and the U-method.

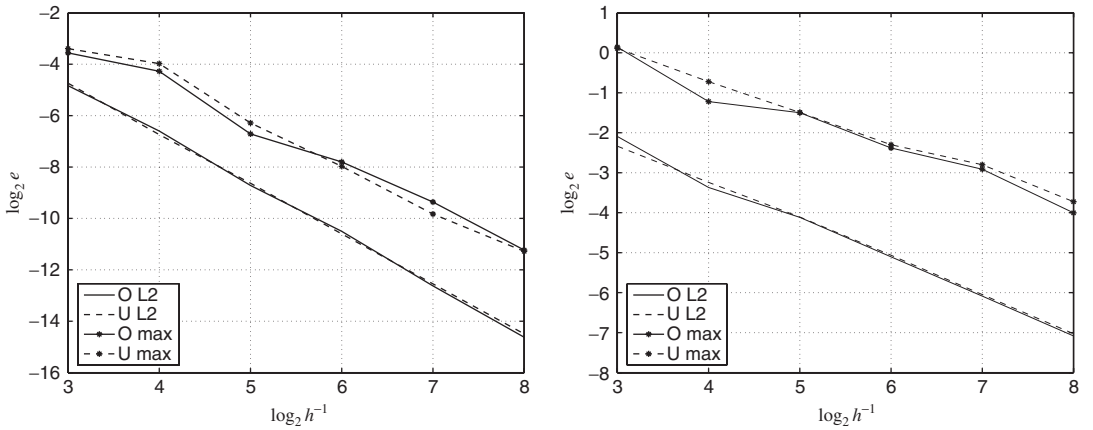

Figure 19. Convergence behaviour for the smooth solution (31) on rough grids.
Left: Pressure. Right: Edge normal flow densities.

The convergence rate is h^2 on smooth as well as on rough grids. This holds both in L^2 norm and in L^∞ norm.

For the normal flow densities, the convergence rate in L^2 norm on smooth grids is h^2 for the O-method, whereas the U-method has a convergence rate $h^{1.6}$. The reduced rate for the U-method seems to stem from the jump in aspect ratio of the grid cells at the boundary, see Figure 17(a). On rough grids the convergence rate drops down to h for both methods. In L^∞ norm the convergence rate for the normal flow densities is h on smooth grids. On rough grids the convergence rate seems to be $\mathcal{O}(h)$ or somewhat lower.

The next test cases are performed on the domain shown in Figure 17(c) where each of the regions labelled 1–4 may have different permeabilities. The permeabilities in regions 1–4 are chosen such that a singularity at the corner where the regions meet, appears. We assume that the medium is isotropic, and use $\omega = 2\pi/3 = 120°$. Let the distance from the corner be r and the angle from the x-axis be θ. In the case where the permeabilities in the regions 2, 3, and 4 are equal, there exists a solution of the form

$$u(r,\theta) = r^\alpha \begin{cases} \cos\alpha(\theta - \pi/3) & \text{for } \theta \in [0, 2\pi/3] \\ d\cos\alpha(4\pi/3 - \theta) & \text{for } \theta \in [2\pi/3, 2\pi] \end{cases} \tag{32}$$

where $\alpha = (3/\pi)\arctan\sqrt{1+2/\kappa}$ and $d = \cos(\alpha\pi/3)/\cos(2\alpha\pi/3)$. Here, $\kappa = k_1/k_2$ is the permeability ratio. For $\kappa \geqslant 0$ exponents $\alpha \in [0.75, 1.5]$ are obtained. Solution (32) belongs to the space $H^{1+\alpha-\varepsilon}$ for any $\varepsilon > 0$.

Two cases with the solution (32) are tested. In the first case $\kappa = 10^{-3}$. This yields $\alpha \approx 1.4787$. The results are shown in Figure 20 for the smooth grids and in Figure 21 for the rough grids. In the second case $\kappa = 10^2$ and $\alpha \approx 0.7547$. The results are shown in Figure 22 for the smooth grids and in Figure 23 for the rough grids.

The convergence rate is the same for both methods. For the pressure, the convergence rate in L^2 norm is $h^{\min\{2,2\alpha\}}$ on smooth as well as on rough grids. In L^∞ norm the convergence

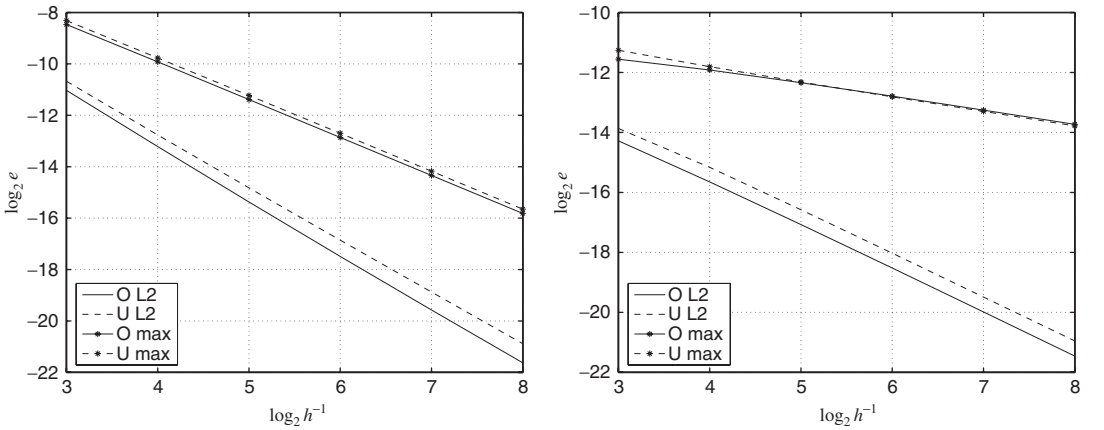

Figure 20. Convergence behaviour for the $H^{2.47}$ solution (32) on smooth grids. Left: Pressure. Right: Edge normal flow densities.

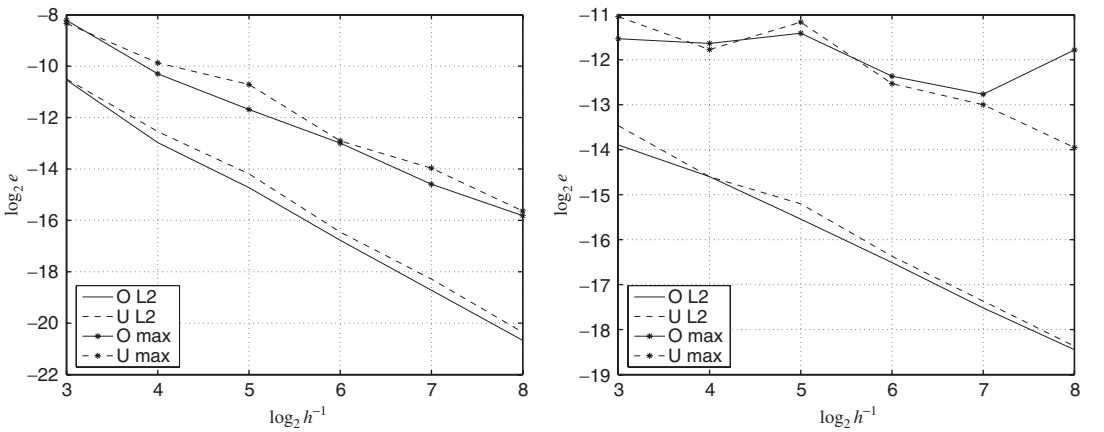

Figure 21. Convergence behaviour for the $H^{2.47}$ solution (32) on rough grids. Left: Pressure. Right: Edge normal flow densities.

rate is h^{α}. This holds on smooth grids, and it also seems to hold on rough grids when the rate is measured over more than one refinement level.

For the normal flow densities, the convergence rate in L^2 norm on smooth grids is h^{α}. On rough grids the convergence rate drops down to h^1 for $\alpha > 1$ and remains at h^{α} for $\alpha \leqslant 1$. In L^{∞} norm the convergence rate on smooth grids is $h^{\alpha-1}$ for $\alpha > 1$. On rough grids convergence cannot be claimed in L^{∞} norm.

If the permeabilities in Figure 17(c) are equal in region 1 and 3, and likewise the permeabilities in region 2 and 4 equal, solutions with lower regularity exist. The solution satisfies

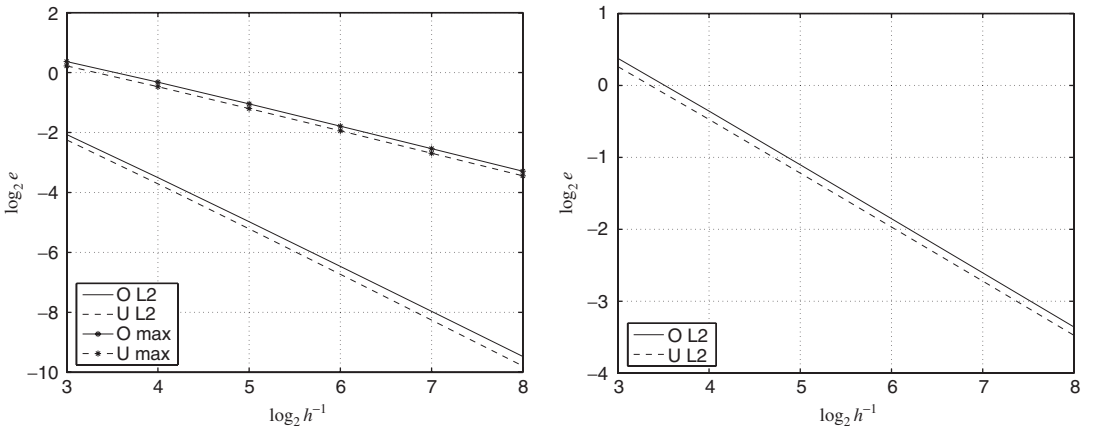

Figure 22. Convergence behaviour for the $H^{1.75}$ solution (32) on smooth grids. Left: Pressure. Right: Edge normal flow densities.

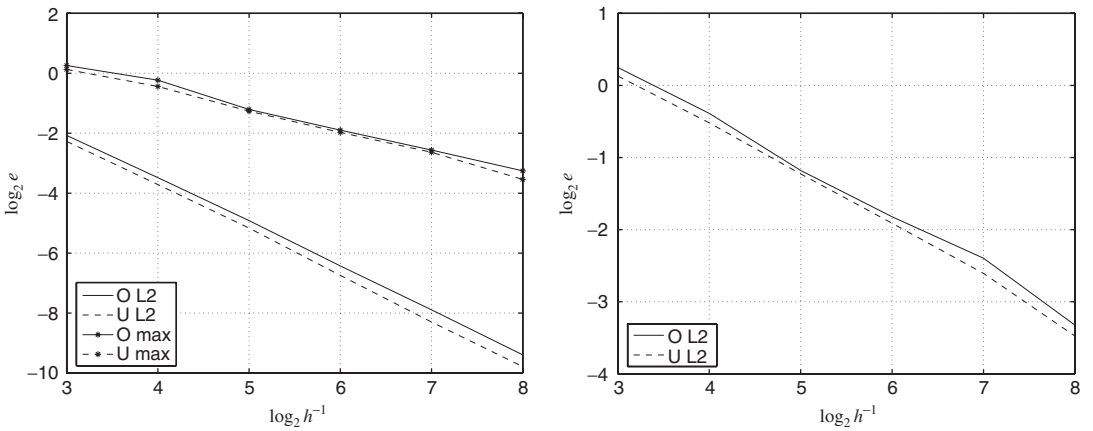

Figure 23. Convergence behaviour for the $H^{1.75}$ solution (32) on rough grids. Left: Pressure. Right: Edge normal flow densities.

$u(r,\theta) = -u(r,\theta-\pi)$ with

$$u(r,\theta) = r^{\alpha}\begin{cases}\cos\alpha(\theta-\pi/3) & \text{for } \theta\in[0,2\pi/3]\\ d\sin\alpha(5\pi/6-\theta) & \text{for } \theta\in[2\pi/3,\pi]\end{cases} \tag{33}$$

Here, $\alpha = (6/\pi)\arctan\left(1/\sqrt{1+2\kappa}\right)$ and $d = \cos(\alpha\pi/3)/\sin(\alpha\pi/6)$. As in the previous test example, $\kappa = k_1/k_2$ is the permeability ratio. For $\kappa \geqslant 0$ exponents $\alpha \in [0, 1.5]$ are obtained, for which solution (33) belongs to the space $H^{1+\alpha-\varepsilon}$ for any $\varepsilon > 0$.

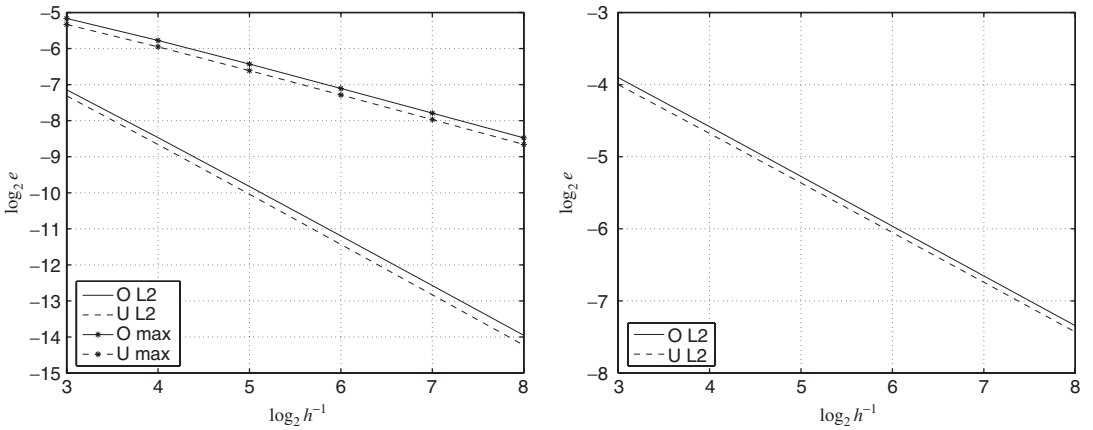

Figure 24. Convergence behaviour for the $H^{1.69}$ solution (33) on smooth grids. Left: Pressure. Right: Edge normal flow densities.

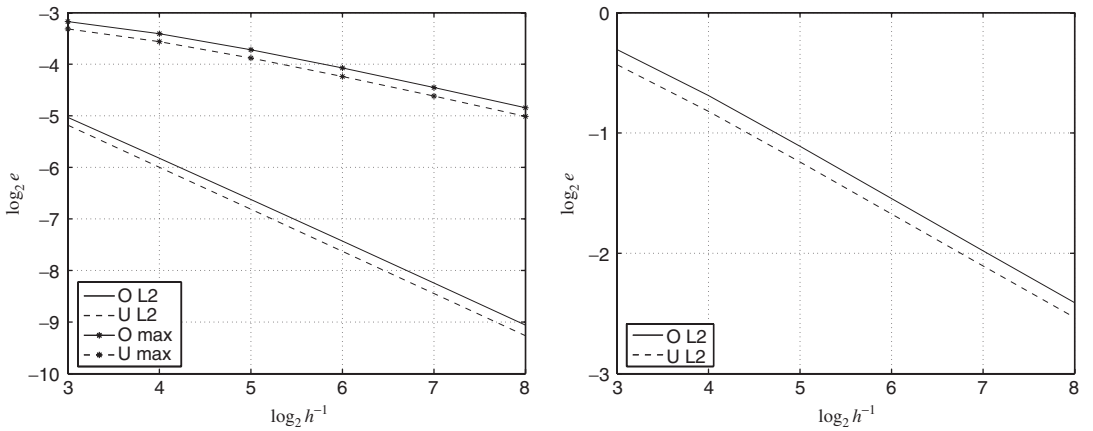

Figure 25. Convergence behaviour for the $H^{1.41}$ solution (33) on smooth grids. Left: Pressure. Right: Edge normal flow densities.

Three cases with solution (33) are tested. These cases are only run on the smooth grid in Figure 17(a). The three cases are given by $\kappa = 3$ ($\alpha \approx 0.6902$), $\kappa = 10$ ($\alpha \approx 0.4103$) and $\kappa = 10^2$ ($\alpha \approx 0.1345$), respectively. The results are shown in Figures 24–26.

The convergence rate is the same for both the O-method and the U-method. For the pressure, the convergence rate in L^2 norm is $h^{2\alpha}$. In L^∞ norm the convergence rate is h^α for the first two cases. The last case ($\alpha \approx 0.1345$) did not reach an asymptotic behaviour on the finest grids and had a reduction by $h^{0.05}$ in the last level. For the normal flow densities, the convergence

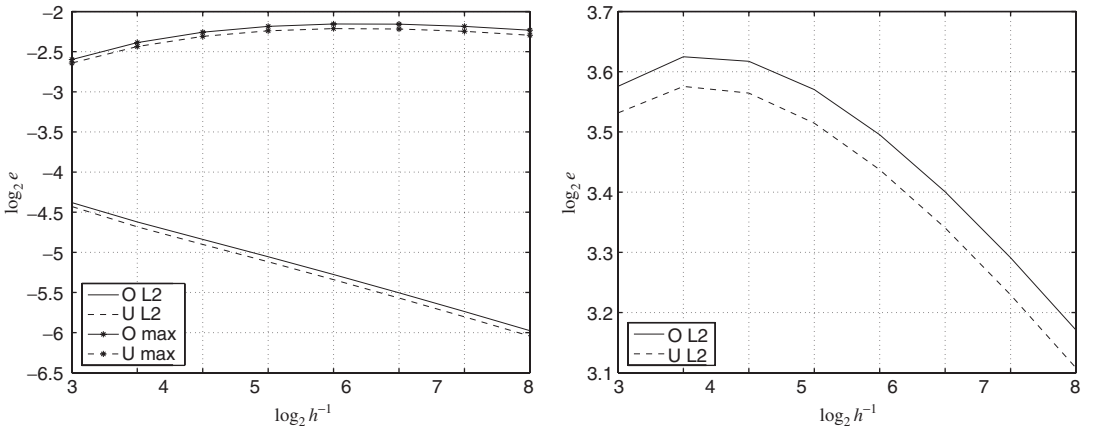

Figure 26. Convergence behaviour for the $H^{1.13}$ solution (33) on smooth grids. Left: Pressure. Right: Edge normal flow densities.

rate in L^2 norm is h^α. However, for the last case ($\alpha \approx 0.1345$) an asymptotic behaviour was not reached until the last refinement level.

In summary, the performed test runs indicate the following error bounds on rough grids:

$$\|u_h - u\|_{L^2} \sim h^{\min\{2,2\alpha\}} \tag{34}$$

$$\|q_h - q\|_{L^2} \sim h^{\min\{1,\alpha\}} \tag{35}$$

$$\|u_h - u\|_{L^\infty} \sim h^{\min\{2,\alpha\}} \tag{36}$$

where $q = \mathbf{q} \cdot \mathbf{n}$ is the normal flow density. For smooth solutions, $\|q_h - q\|_{L^\infty}$ seems to be $\mathcal{O}(h)$ or somewhat lower, but the test runs do not clarify the regularity required to reach this convergence rate.

On smooth grids, the convergence rates for the pressure is the same as for rough grids. For the normal flow densities, however, an increased convergence rate is observed

$$\|q_h - q\|_{L^2} \sim h^{\min\{2,\alpha\}} \tag{37}$$

$$\|q_h - q\|_{L^\infty} \sim h^{\min\{1,\alpha-1\}}, \quad \alpha > 1 \tag{38}$$

Due to boundary effects, however, the highest convergence rate of Equation (37) may be lower than h^2 for the U-method.

The L^∞ convergence rates which are indicated above, must be taken with precaution. For example, it is by no means clear that only the Sobolev-space regularity and the grid smoothness determine the L^∞ convergence rates. A property like the monotonicity of the method [21] might be important for these convergence rates.

5. THREE-DIMENSIONAL RESULTS

Next, numerical test runs on three-dimensional grids in physical space will be performed. When going from two dimensions to three dimensions, the general positioning of corners of the control volumes implies that bilinear cell surfaces may arise. These surfaces may for some methods create additional difficulties for handling of fluxes across cell interfaces [22]. In particular, methods that rely on a transformation from the physical grid to an orthogonal reference grid will not be able to reproduce uniform flow exactly.

This is not the case with the O-method discretization in physical space. As an example, a 3D grid created by random h perturbations of the corners in all directions of an initial orthogonal grid, is shown in Figure 27. The numerical pressure is exact to working precision (10^{-16}) when uniform flow is used as a reference test for arbitrary conforming grids. This is explained by the way the transmissibilities are derived in 3D in physical space. The term $-\int_S \mathbf{n}^{\mathrm{T}}\mathbf{K}\,\mathrm{grad}\,u\,\mathrm{d}\sigma$ for each edge is discretized by the assumption of piecewise linear pressure. The normal vector $\mathbf{n}$ is parametrized by (25) for general bilinear surfaces, and $-\int_S \mathbf{n}\,\mathrm{d}\sigma$ is hence exact by (26). For linear pressure, $\mathrm{grad}\,u$ is constant, and the flux discretization that the transmissibility calculations apply, is therefore exact. Together with the uniform flow result for 2D cases in Reference [16], this then implies that the pressure solution for the O-method in 3D is exact for uniform flow, and is verified by our numerical results.

A case of nonuniform flow is next tested for our 3D implementation of the O-method. It is trivial to verify that the function

$$u(x, y, z) = \sin(\sqrt{2}\pi x)\sinh(\pi y)\sinh(\pi z) \tag{39}$$

is a solution to problem (1) when the medium is isotropic and homogeneous. The L^2 convergence is examined for both the pressures and normal flow densities for the set of i-edges in a 3D grid similar to that of Figure 27. The results are depicted in Figure 28 for different grids. Dirichlet boundary conditions which correspond to the reference solution above, are implemented by interpolation. The first test shows the numerical results for uniform refinement of

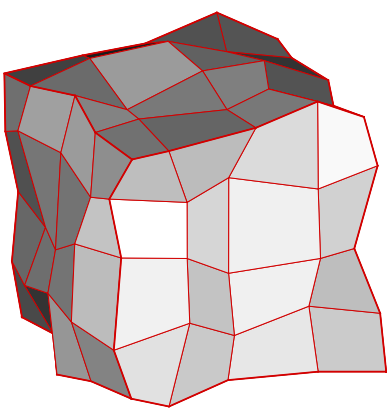

Figure 27. 3D grid. All corners perturbed randomly in x, y, and z direction.

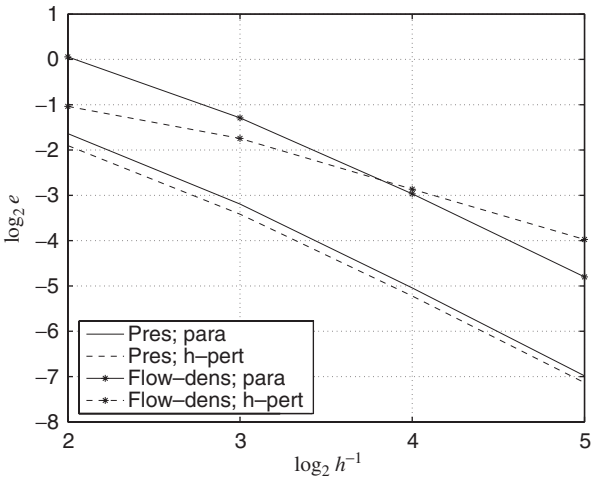

Figure 28. Convergence in L^2 norm for pressure and edge normal flow densities of i-edges of grids in 3D.

parallelepiped grids on a fixed domain. As is expected, both the pressure and normal flow densities converge as h^2 when the grid is refined uniformly.

The second test shows the convergence behaviour for an orthogonal initial grid for which all corners are arbitrarily perturbed by terms of order h in all directions (for which nonoverlapping grid cells do not occur). The pressure still converges as h^2, but the normal flow density convergence decreases to h, which is expected from the results in 2D.

The 3D test runs agree with the conclusions for the convergence rates in 2D.

6. CONCLUSIONS

We have presented numerical convergence tests for the MPFA O-method and U-method. The test examples indicate that these methods have equal convergence rates, though boundary effects may reduce the highest convergence rate for the normal flow densities in the U-method. If the pressure is in $H^{1+\alpha}$, $\alpha > 0$, the found L^2 convergence order on rough grids is $\min\{2, 2\alpha\}$ for the pressure and $\min\{1, \alpha\}$ for the normal flow densities. For smooth grids the convergence order for the normal flow densities increases to $\min\{2, \alpha\}$ for the O-method.

The O-method is exact for uniform flow on rough grids. This also holds in three dimensions, where the cells may have nonplanar surfaces.

REFERENCES

1. Aavatsmark I. Introduction to multipoint flux approximations for quadrilateral grids. *Computational Geosciences* 2002; **6**:405–432.
2. Aavatsmark I. Mehrpunktflussverfahren, http://www.mi.uib.no/~aavat/mpfa.pdf
3. Aavatsmark I, Barkve T, Bøe Ø, Mannseth T. Discretization on non-orthogonal, quadrilateral grids for inhomogeneous, anisotropic media. *Journal of Computational Physics* 1996; **127**:2–14.

4. Aavatsmark I, Barkve T, Mannseth T. Control-volume discretization methods for 3D quadrilateral grids in inhomogeneous, anisotropic reservoirs. *SPE Journal* 1998; **3**:146–154.
5. Aavatsmark I, Eigestad GT, Klausen RA. Numerical convergence of the MPFA O-method for general quadrilateral grids in two and three dimensions. In *Compatible Spatial Discretizations*, Arnold DN, Bochev PB, Lehoucq R, Nicolaides RA, Shashkov M (eds), IMA Volume Series. Springer: New York, 2006; 1–21, in press.
6. Edwards MG, Rogers CF. Finite volume discretization with imposed flux continuity for the general tensor pressure equation. *Computational Geosciences* 1998; **2**:259–290.
7. Aavatsmark I, Barkve T, Bøe Ø, Mannseth T. A class of discretization methods for structured and unstructured grids in anisotropic, inhomogeneous media. In *Proceedings of the 5th European Conference on the Mathematics of Oil Recovery*, Heinemann ZE, Kriebernegg M (eds), Leoben, Austria, 1996; 157–166.
8. Aavatsmark I, Barkve T, Bøe Ø, Mannseth T. Discretization on unstructured grids for inhomogeneous, anisotropic media. Part I: Derivation of the methods. *SIAM Journal on Scientific Computing* 1998; **19**: 1700–1716.
9. Aavatsmark I, Barkve T, Bøe Ø, Mannseth T. Discretization on unstructured grids for inhomogeneous, anisotropic media. Part II: Discussion and numerical results. *SIAM Journal on Scientific Computing* 1998; **19**:1717–1736.
10. Edwards MG. Unstructured, control-volume distributed, full-tensor finite-volume schemes with flow based grids. *Computational Geosciences* 2002; **6**:433–452.
11. Verma S, Aziz K. Two- and three-dimensional flexible grids for reservoir simulation. In *Proceedings of the 5th European Conference on the Mathematics of Oil Recovery*, Heinemann ZE, Kriebernegg M (eds), Leoben, Austria, 1996; 143–156.
12. Nordbotten JM, Eigestad GT. Discretization on quadrilateral grids with improved monotonicity. *Journal of Computational Physics* 2005; **203**:744–760.
13. Ware AF, Parrott AK, Rogers C. A finite volume discretization for porous media flows governed by non-diagonal permeability tensors. In *Proceedings of CFD95*, Thibault PA, Bergeron DM (eds), Banff, Canada, 1995; 357–364.
14. Klausen RA, Russell TF. Relationships among some locally conservative discretization methods which handle discontinuous coefficients. *Computational Geosciences* 2004; **8**:341–377.
15. Klausen RA, Winther R. Convergence of multi point flux approximations on quadrilateral grids. *Numerical Methods for Partial Differential Equations*, submitted.
16. Eigestad GT, Klausen RA. On the convergence of the multi-point flux approximation O-method; Numerical experiments for discontinuous permeability. *Numerical Methods for Partial Differential Equations* 2005; **21**:1079–1098.
17. Hyman J, Shashkov M, Steinberg S. The numerical solution of diffusion problems in strongly heterogeneous non-isotropic materials. *Journal of Computational Physics* 1997; **132**:130–148.
18. Mishev ID. Nonconforming finite volume methods. *Computational Geosciences* 2002; **6**:253–268.
19. Shashkov M, Steinberg S. Solving diffusion equations with rough coefficients in rough grids. *Journal of Computational Physics* 1996; **129**:383–405.
20. Strang G, Fix GJ. *An Analysis of the Finite Element Method.* Wiley: New York, 1973.
21. Nordbotten JM, Aavatsmark I. Monotonicity conditions for control volume methods on uniform parallelogram grids in homogeneous media. *Computational Geosciences* 2005; **9**:61–72.
22. Naff RL, Russel TF, Wilson JD. Shape functions for velocity interpolation in general hexahedral cells. *Computational Geosciences* 2002; **6**:285–314.

